SYNTHESIS AND CHARACTERIZATION OF DOPED Cu^{2+}-Bi_2O_3 NANOPARTICLES AND IT'S ANTIBACTERIAL ACTIVITY

E. Tamilnidhi[1], G. Lakshiminarayanan[2], S. Arumugam[3]
D.Gopinath[4]

[1,2,3]Department of Physics, Shanmuga Industries Arts & Science College, Affiliated to Thiruvalluvar University, Tiruvannamalai, Tamilnadu-606603, India
[4]Department of Physics, Mailam Engineering College, Mailam, Villupuram Tamilnadu, India

[1]E-mail id: tamilnithiphy@shanmugacollege.edu.in
[2]E-mail id: lakshminarayananphy@shanmugacollege.edu.in
[3]E-mail id: arumugamphy@ shanmugacollege.edu.in
[4]E-mail id: gopinathphysics@mailamengg.com
Corresponding Author: G. Lakshiminarayanan*

Abstract

Pure bismuth oxide (Bi_2O_3) and copper-doped bismuth oxide (Cu_2O_3 with 1% and 3% Cu) nanoparticles were successfully synthesized by a chemical precipitation method. The synthesized nanoparticles were characterized using X-ray diffraction (XRD), FT-IR, UV–Visible spectroscopy, photoluminescence (PL), scanning electron microscopy coupled with energy-dispersive X-ray analysis (SEM-EDAX), high-resolution transmission electron microscopy (HR-TEM), and antibacterial studies. XRD analysis confirmed the incorporation of Cu ions into the α-Bi_2O_3 lattice, exhibiting a tetragonal crystal structure. SEM images revealed rod-shaped microstructures for pure Bi_2O_3, whereas Cu doping resulted in distorted and fragmented rods. EDAX confirmed the elemental composition of the synthesized samples. FT-IR spectra identified the characteristic functional groups and bonding features. UV–Vis analysis showed strong absorption in the 200–800 nm range with a prominent peak at 382 nm. PL spectra exhibited emission peaks at 435 and 475 nm. Antibacterial activity against Escherichia coli demonstrated the potential biomedical application of the nanoparticles.

Keywords: Bi_2O_3nanoparticles, Cu-doping, Structural studies, Morphology, Antibacterial Activity.

How to cite this article: Tamilnidhi E, Lakshiminarayanan G, Arumugam S, Gopinath D. Synthesis and characterization of doped Cu2+-Bi2O3 nanoparticles and its antibacterial activity. Int J Drug Deliv Technol. 2026;16(74s): 1752-1758. DOI: 10.25258/ijddt.16.74s.146

1. Introduction

Semiconductor nanomaterials have attracted considerable attention due to their applications in solar energy conversion, environmental remediation, catalysis, and biomedical technologies. Among them, bismuth oxide (Bi_2O_3) is an important semiconductor owing to its high oxygen-ion conductivity, excellent photoconductivity, photoluminescence, and chemical stability. These properties make it suitable for applications such as gas sensors, solid oxide fuel cells, photocatalysts, optical coatings, and optoelectronic devices [1–4].

Bi_2O_3 exists in several polymorphic forms, including α-, β-, γ-, δ-, and ω-Bi_2O_3 [5-7]. Among these phases, β-Bi_2O_3 exhibits strong visible-light absorption and enhanced photocatalytic performance due to its relatively narrow band gap [8-10]. The structural, optical, and electronic properties of Bi_2O_3 can be further tailored through transition-metal doping, which influences particle size, morphology, and charge-carrier dynamics.

Various techniques have been employed for the synthesis of Bi_2O_3 nanoparticles, including hydrothermal, sol–gel, and chemical precipitation methods. Among them, chemical precipitation is widely used because of its simplicity, low cost, and ability to produce nanoparticles with controlled morphology and size [11–13].

Bismuth compounds are known for their low toxicity and antibacterial properties, making Bi_2O_3 nanoparticles attractive for biomedical applications [14–17]. In the present study, pure and Cu-doped Bi_2O_3 nanoparticles (1% and 3% Cu) were synthesized by a chemical precipitation method. Their structural, morphological, optical, and antibacterial properties were systematically investigated using XRD, FT-IR, UV–Vis, PL, SEM-EDAX, HR-TEM, and antibacterial activity analyses.

2. Materials and Methods

2.1. Chemicals

For this study Bismuth (III) nitrate pentahydrate (Bi $(NO_3)_3$ $5H_2O$), Nitric Acid (HNO_3), Sodium Hydroxide (NaOH) and – Copper Acetate ($C_4H_6CuO_4{\cdot}H_2O$) were used. All chemical reagents are standard analytical grade and used without further treatment. All

solutions used in the experiments were prepared using distilled water as solvent.

2.2. Preparation of Pure and Cu doped Bi_2O_3 Nanoparticles

For the synthesis of Bi_2O_3 Nano particles, Bismuth Nitrate was used as a precursor. For pure Bi_2O_3, 0.2 M of Bismuth (III) nitrate pentahydrate Bi $(NO_3)_3$ $5H_2O$ was dissolved in 25 ml of deionized water and then stirred the solution vigorously. A white precipitate appeared immediately during water dilution to 0.3 M of Nitric acid (HNO_3) dissolved in 25 ml of deionized water was added drop wise to the above solution under stirring. The amount of $NO3^-$ groups was supposed to be the factor affecting the solubility of Bi $(NO_3)_3 5H_2O$ because the pH values were extremely acidic (pH < 1) and stayed approximately invariant during the water dilution. During the NaOH titration process, 0.2 mole of NaOH pellet were dissolved in 50 ml of de-ionized water. The Sodium hydroxide solution was added drop wise into the solution then white precipitate was appeared. The mixed solution was heated at 60 °C and continuously stirred for 5 hr, after that the yellow colour was obtained. The fabricated yellow precipitate was filtration and washed with double distilled water and ethanol several times to remove possible impurities before being dried in an oven at 100 °C for 1 h in oven and then the product was annealed at 400 °C in muffle furnace for 6 h to get phase pure Bismuth Oxide nanopowders. The same procedure was used for the synthesis of Cu doped (1 and 3 mol %) Bi_2O_3 Nanoparticles with adding copper acetate.

2.3. Method for Antibacrial activity

In *Antibacrial* activity, the materials used for bismuth oxide nanoparticle sample, Escherichia coli, Agar-agar 0.5g, Nutrient agar 5.6g, Nutrient broth 1.3g, antibiotic discs, petri plates and cotton swabs. Disc diffusion methods used for antimicrobial activity of bismuth oxide nanoparticles were studied. After the nutrient agar was made, it was added to the sterile Petri dishes and left to solidify. It was swabbed with 24-hour-growing E. Coli bacterial cultures. A cork borer was used to create the five wells (10 mm in diameter). The nanoparticles were put into the wells at four different doses (50 µg, 100 µg, 200 µg, and 1000 µg) along with tetracycline as a negative control. The plates were then incubated for a 24 hour at 37 ºC.

2.4. Characterization

The preparation of pure and doped Cu^{2+}-Bi_2O_3 NPs were characterized using X-ray diffraction (X'PERT PRO diffractometer with Cu-Ka radiation (k = 1.5406 Å). The range of 2θ angles is from 10° to 90°. The X-Ray tube is operated at 40kV, 30 mA with a scanning speed of 0.05 second per step. Experimentally the obtained diffraction pattern of the sample is compared with Joint Committee on Powder Diffraction Standard (JCPDS) data.

The crystalline size (D) of the particles were determined from the XRD line broadening measurement using Scherrer equation,

$$D = \frac{k\lambda}{\beta cos\theta}$$

Where D is the average crystallite diameter (Å), K is the Scherrer's constant (0.941), λ is the wavelength (1.5406 Å), β is the full width at half maximum, δ is the dislocation density, E_{stain} is the microstain and θ is the Bragg's angle. From this XRD patterns analysis, we have observed peak intensity, position and width, full-width at half-maximum (FWHM) data. Using the KBr pellet technique, Fourier transform infrared spectroscopy (FT-IR) analysis (SHIMADZU-8400 with a resolution of 4 cm-1) carried out for the prepared powders. The scan was recorded between 400 and 4000 cm^{-1}. For the prepared samples, scanning electron microscopy was performed using a JEOL JSM-6390, Japan microscope. For the pure and doped Cu2+-Bi2O3 powders, the scan was carried out at high vacuum mode with an accelerating voltage of 30 kV, a working distance of 10 mm, and magnifications of X 2000 and 3000. Energy dispersive X-ray spectra (EDX. JEOL/EO, Japan) were used to analyze the elements in the prepared samples. The Ultraviolet–Visible absorbance spectroscopy (UV–vis) was conducted using a SHIMADZU UV -1650 model. The analytical range was measured at various wavelengths between 350 and 800 nm. The Photoluminescence spectra (PL) were performed using a (Jobin Yvon, FLUOROLOG-FL3-11) with a He-Cd 280 nm laser as an excitation source.

3. Results and Discussion

3.1. Structural Analysis (X-ray diffraction)

The XRD spectra of pure Cu^{2+} doped (1% and 3%) Bi_2O_3 NPs are shown in Fig. 1. The major peaks of Cu^{2+} doped Bi_2O_3 NPs at reflection plane values of (210), (201), (211), (220), (212), (222) (421) and (402) were equal to corresponding 2θ values 25.83º, 27.41º, 30.37º, 33.22º, 42.30º, 46.30º, 56.01º and 58.96º respectively which are attributed to the form nanoparticles.

All diffractions peaks of the obtained product are corresponding to the tetragonal structure with lattice constants a = b = 3.256 Å and c = 5.207 Å (JCPDS card number: 27-0050). The lack of Cu^{2+} peaks in Cu^{2+}-doped Bi_2O_3 NPs may be caused by the lower ionic radius of Cu^{2+} ions (0.057 nm) in comparison to Bi^{3+} ions (0.103 nm) and the low concentration of Cu^{2+} (1% and 3%). The crystallite size of pure Bi_2O_3, 1% Cu^{2+}-Bi_2O_3, and 3% Cu^{2+}-Bi_2O_3 NPs was 65, 62, and 53 nm, respectively. The reduction in size upon Cu^{2+}-doping was because of the smaller ionic radius of Cu^{2+} than those of Bi^{3+}.

The particle sizes of Bi_2O_3 NPs were decreased after Cu^{2+} doping [18].

3.2. UV- visible spectral analysis

The UV-Vis absorption spectrums of pure Cu^{2+} doped (1% and 3%) Bi_2O_3 NPs were synthesized by chemical precipitation method as shown in Fig.2. The optical absorption coefficient was calculated in the wavelength range of 200-800 nm. The UV-visible results show red shift absorption at ~382 nm, ~386 nm and ~390 for pure and Cu^{2+} doped (1% and 3%) Bi_2O_3 NPs [19,20].

The high intensity of UV-vis spectra clearly showed a high intensity of pure and doped bismuth oxide NPs present in the samples. The energy band gap of the Bi_2O_3 were calculated using the relation,

$$E_g = \frac{hc}{\lambda}\ eV$$

Where Eg is the band gap energy (eV), h is the Planck's constant (6.626×10^{-34} Js), c is the light velocity (3×10^{8} m/s) and λ is the Wavelength (nm). The band gap energy (Eg) calculated from pure and Cu^{2+} doped (1% and 3%) Bi_2O_3 NPs is 3.24 eV, 3.21 eV and 3.17 eV respectively [21].

3.3. PL Spectroscopy

The room-temperature PL spectra of pure and Cu^{2+} doped (1 and 3%) Bi_2O_3 NPs with a 382 nm as an excitation wavelength are given in UV-Vis spectra are shown in Fig. 3. The visible emission peaks at 435, 452, and 475 nm are observed for all the prepared NPs. However, intensity of Cu-doped Bi_2O_3 NPs decreases with increasing Cu concentrations. Lower intensity of 3% Cu^{2+} Bi_2O_3 NPs suggested the effective migration of charge carriers (electron and holes) from the inner part of NPs to the surface so that they can participate in surface redox reactions [18]. The PL spectra show that the effect of doped impurities on photogenerated charge recombination varied according to impurity quantity. The PL results showed that impurity doping can reduce the recombination of photogenerated holes and electrons, which is favorable to the photocatalytic activity [28,29].

3.4. FT-IR Analysis

The FT-IR spectra of the pure and Cu^{2+} doped (1 and 3%) Bi_2O_3 NPs are shown in Fig. 4. It is a method which may employ to establish the presence of chemical functional groups in sample. The findings of bismuth oxide nanoparticles, FT-IR spectrum gathering between 4000– 500 cm^{-1} are displayed in the figure. The absorption peak at 3464 cm^{-1} believed to be associated with the stretching vibrations of hydrogen bonded surface water molecules and hydroxyl groups. The lower absorption peaks at 3011 cm^{-1} corresponds to the C-O molecule is responsible for the IR bands. The medium peaks at 1673 cm^{-1} are attributed to the presence of C=O stretching. The bands occurring near 700-400 are attributed to the vibration of Bi-O-Bi & Cu bonds. The vibration band at 1200-1700 cm^{-1} is a distinguishing property of the NO_3- group (Bi_2O_3).The band at 980 cm^{-1} and 520 cm^{-1} is attributed to the M–O blending vibration bonding, which contribute to the formation of pure and synthetic metal oxides [22,23,24].

3.5. Surface and Morphological analysis

The crystalline shape and surface morphology of the pure and pure and Cu^{2+} doped Bi_2O_3 NPs were determined by using SEM analysis as shown in the supplementary Fig.5 a & b. The micrograph images (SEM) of pure and Cu^{2+} doped Bi_2O_3 nanoparticles prove that they are in nanoscale range (smaller size or 10^{-9} m) aggregated, spherical shape and uneven surface morphology observed. The aggregation usually occurs when synthesis is carried out in aqueous medium and also possibly due to densification resulting in narrow space between particles. The presence of elemental compositions bismuth, oxygen and copper were identified by EDAX spectra. The major peaks for Bismuth (Bi) and Oxygen (O) confirm the presence of bismuth oxide nanoparticles [26,27]. The small peaks for copper were observed in presence of cu doped bismuth oxide nanoparticles as shown in Fig. 5 c & d.

In TEM study, the morphology, microstructure and particle size of synthesized samples and were characterized by TEM. The supplementary Fig. 6 a & b shows the TEM images of pure and 3% Cu− Bi_2O_3 NPs. These TEM images display that prepared NPs possess spherical morphology with some degrees of agglomeration. The shape of Bi_2O_3 NPs remains the same but particle size decreases after Cu-doping (65−53 nm), which is in agreement with size estimated from the Scherrer equation. The tetragonal structure of Bi_2O_3 NPs is further confirmed by the visible lattice fringes as shown in supplementary Fig. 6 c & d. These images demonstrate the presence of both Bi_2O_3 and Cu with high-quality lattice fringes without distortion. The interplanar spacing of the lattice of Bi_2O_3 NPs and 3% Cu− Bi_2O_3 NPs is 0.2094 nm and 0.2089 nm, respectively, which relates to the (201) plane of the tetragonal phase of Bi_2O_3, whereas the lattice fringe of Cu has an interplanar spacing of 0.19 nm which corresponds to the (220) plane of the monoclinic Cu crystallographic structure[25].

3.6. Antibacterial Activity

The disc diffusion method has been adopted to investigate the antibacterial activity of pure and Cu2+ doped Bi_2O_3 NPs against

human pathogens. The antibacterial activity was performed against Escherichia colli bacterial pathogens for three different concentrations 1, 2, 3 (50, 100, 200 µg/ml) and 4, 5 are control and antibiotic of pure and copper doped bismuth NPs is shown in supplementary Fig. 7 (a),(b) & (c). In addition, doped sample showed higher activity on zone of inhibition it has better antibacterial activity when compared to pure may be attributed to its smaller particle sizes. Particle sizes and morphology play an important role in the antibacterial activity of metal oxide nanoparticles. Generally, antibacterial activity of metal oxide nanoparticles is due to the interaction of nanoparticles on to the bacterial cell wall by electrostatic attraction between the negatively charged bacteria and positively charged nanoparticles [30]. In this interaction not only inhibit the bacterial growth and induce the reactive oxygen species (ROS) generation, which leads to cell death.

The actual mechanism of antibacterial activity of Bi_2O_3 NPs takes place on the interfere with the bacteria cell membrane and binding with mesosome will there by disturb the mesosomal functions of cellular respiration, DNA replication, cell division and increased the surface area of bacterial cell membrane these intracellular functional changes of oxidative stress induced by ROS generation due to the cell expiry.

4. Conclusion

Pure and Cu-doped Bi_2O_3 nanoparticles were successfully synthesized using a chemical precipitation method. The structural, morphological, optical, and antibacterial properties of the synthesized nanoparticles were investigated using XRD, FT-IR, UV–Vis, PL, SEM-EDAX, and HR-TEM techniques. XRD analysis confirmed the formation of crystalline tetragonal Bi_2O_3, while Cu doping reduced the crystallite size. UV–Vis studies revealed absorption peaks at 382, 386, and 390 nm for pure, 1%, and 3% Cu-doped Bi_2O_3 nanoparticles, respectively, with corresponding band gap energies of 3.24, 3.21, and 3.17 eV. FT-IR spectra confirmed the characteristic metal–oxygen bonding, whereas SEM and HR-TEM analyses demonstrated nanoscale morphology and successful incorporation of Cu into the Bi_2O_3 lattice. PL spectra exhibited emission peaks at 435 and 475 nm. Furthermore, Cu-doped samples showed enhanced antibacterial activity against Escherichia coli, indicating their potential for antimicrobial and biomedical applications.

References

1. N. Karim, S. Liu, A.K. Rashwan, J. Xie, J. Mo, A.I. Osman, D.W. Rooney, W. Chen, *Int. J. Biol. Macromol.*, 247, 125839 (2023). https://doi.org/10.1016/j.ijbiomac.2023.125839
2. Sh. Labib, *J. Saudi Chem. Soc.*, 21(6), 664–672 (2017). https://doi.org/10.1016/j.jscs.2016.05.002
3. R.K. Jha, R. Pasricha, V. Ravi, *Ceram. Int.*, 31, 495–497 (2005). https://doi.org/10.1016/j.ceramint.2004.06.015
4. K. Li, C. Yang, Y. Xu, D. Ying, Y. Wang, J. Jia, *Chem. Eng. J.*, 211, 208–215 (2013). https://doi.org/10.1016/j.cej.2012.09.094
5. J. Yan, J. Lu, Y. Sheng, Y. Sun, D. Zhang, *Micromachines*, 15(7), 849 (2024). https://doi.org/10.3390/mi15070849
6. Y. Yoon, P.L. Truong, D. Lee, S.H. K., *ACS Nanoscience Au*, 2, 64–92 (2022). https://doi.org/10.1021/acsnanoscienceau.1c00043
7. N.N. Rosman, M.Y. Rozan, M.S.N.R. Adawiyah, et al., *Int. J. Energy Res.*, (2022). https://doi.org/10.1002/er.8001
8. V. Mane, D. Dake, N. Raskar, R. Sonpir, E. Stathatos, B. Dole, *Chem. Phys. Impact*, 8, 100517 (2024). https://doi.org/10.1016/j.chphi.2023.100517
9. M.S. Chavali, M.P. Nikolova, *SN Appl. Sci.*, 1(6), 607 (2019). https://doi.org/10.1007/s42452-019-0592-3
10. D.P. Dutta, M. Roy, A.K. Tyagi, *Dalton Trans.*, 41, 10238–10248 (2012). https://doi.org/10.1039/C2DT30738K
11. Y. Wu, Y.-C. Chaing, C.-Y. Huang, S.-F. Wang, *Dyes Pigments*, 98, 25–30 (2013). https://doi.org/10.1016/j.dyepig.2013.03.009
12. I. Ramli, M.N.N. Nasriah, Y.H. Taufiq-Yap, S.B.A. Hamid, *Catal. Today*, 93–95, 701–709 (2004). https://doi.org/10.1016/j.cattod.2004.06.054
13. H.F. Cheng, B.B. Huang, J.B. Lu, et al., *Phys. Chem. Chem. Phys.*, 12, 15468–15475 (2010). https://doi.org/10.1039/C0CP00555A
14. E.A. Marcus, G. Sachs, D.R. Scott, *Aliment. Pharmacol. Ther.*, 42, 922–933 (2015). https://doi.org/10.1111/apt.13363

15. M. Bartoli, P. Jagdale, A. Tagliaferro, *Materials*, 13, 5234 (2020). https://doi.org/10.3390/ma13225234
16. M. Ahamed, M.J. Akhtar, M.A.M. Khan, Z.M. Alaizeri, H. Alhadlaq, *ACS Omega*, 6, 17353–17361 (2021). https://doi.org/10.1021/acsomega.1c02014
17. J. Wang, X. Yang, K. Zhao, et al., *J. Mater. Chem. A*, 1(32), 9069–9074 (2013). https://doi.org/10.1039/C3TA11565E
18. P. Malathy, K. Vignesh, M. Rajarajan, A. Suganthi, *Ceram. Int.*, 40, 101–107 (2014). https://doi.org/10.1016/j.ceramint.2013.06.030
19. D. Saritha, Y. Markandeya, M. Salagram, et al., *J. Non-Cryst. Solids*, 354, 52–54 (2008). https://doi.org/10.1016/j.jnoncrysol.2007.07.060
20. K.K. Bera, M. Majumdar, M. Chakraborty, S.K. Bhattacharyya, *J. Hazard. Mater.*, 352, 182–191 (2018). https://doi.org/10.1016/j.jhazmat.2018.03.036
21. F.S. Ali, M. Ragamathunnisa, F. Al Marzouqi, et al., *J. Optoelectron. Biomed. Mater.*, 13(3), 95–106 (2021).
22. H.Y. Jiang, K. Cheng, J. Lin, *Phys. Chem. Chem. Phys.*, 14(35), 12114–12121 (2012). https://doi.org/10.1039/C2CP41612A
23. C.K. Lo, D. Xiao, M.M.F. Choi, *J. Mater. Chem.*, 17, 2418–2427 (2007). https://doi.org/10.1039/B702415A
24. M. Mallahi, A. Shokuhfar, M.R. Vaezi, et al., *Am. J. Eng. Res.*, 3, 162–165 (2014).
25. X. Liu, H. Cao, J. Yin, *Nano Res.*, 4, 470–482 (2011). https://doi.org/10.1007/s12274-011-0107-5
26. M.R. Mozdianfard, F. Masoodiyeh, J. Karimi-Sabet, *J. Supercrit. Fluids*, 136, 144–156 (2018). https://doi.org/10.1016/j.supflu.2018.02.020
27. M. Ahamed, M.A.M. Khan, M.J. Akhtar, et al., *Sci. Rep.*, 6, 30196 (2016). https://doi.org/10.1038/srep30196
28. B. Perillo, M. Di Donato, A. Pezone, et al., *Exp. Mol. Med.*, 52, 192–203 (2020). https://doi.org/10.1038/s12276-020-0383-8
29. F. Ciccarese, V. Raimondi, E. Sharova, et al., *Antioxidants*, 9, 211 (2020). https://doi.org/10.3390/antiox9030211
30. P. Magesan, A. Sviaranjani, *Int. J. Pure Appl. Math.*, 119(2), 6345–6359 (2018).

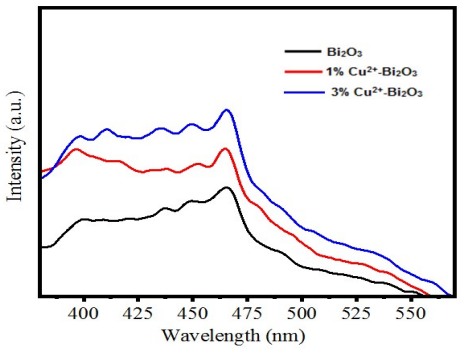

Figure Captions

Fig.1. XRD pattern for pure and Cu^{2+} doped Bi_2O_3 NPs.
Fig.2. UV-Vis spectrum of pure and Cu^{2+} doped Bi_2O_3 NPs.
Fig. 3. PL spectrum of pure and Cu^{2+} doped Bi_2O_3 NPs.
Fig. 4. FT-IR spectra of pure and Cu^{2+} doped Bi_2O_3 NPs.

Fig .1

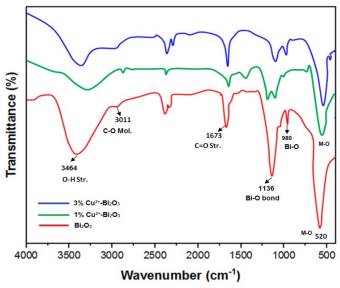

Fig .2

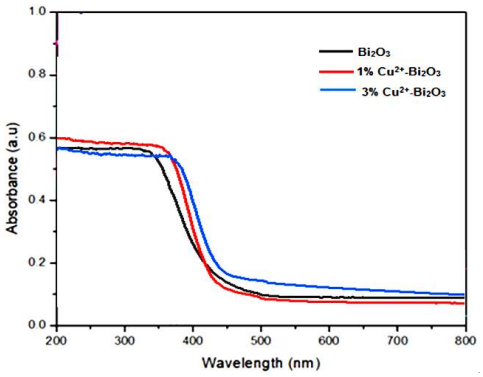

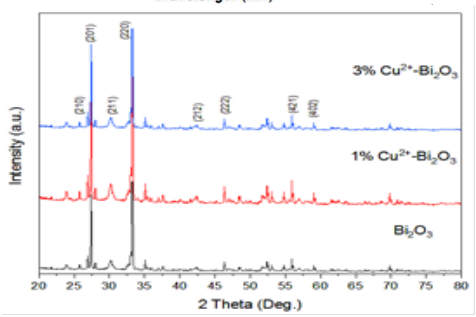

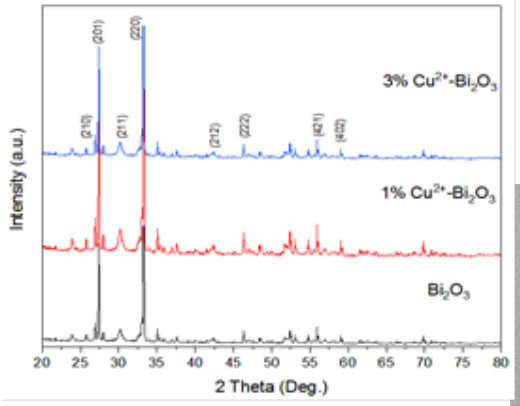

Fig .3

Supplementary Figure Captions

Fig. 5(a)(b)(c)(d). SEM image of pure and Cu^{2+} doped Bi_2O_3 NPs. with EDAX spectrum.

Fig. 6(a)(b). TEM image of pure and Cu^{2+} doped Bi_2O_3 NPs with lattice fringes.

Fig. 7(a)(b)(c). Antibacterial activity of pure and Cu doped Bi_2O_3 NPs and zone of inhibition values for different concentration.

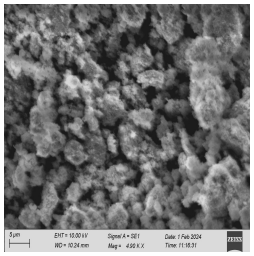

Fig. 5 (a)

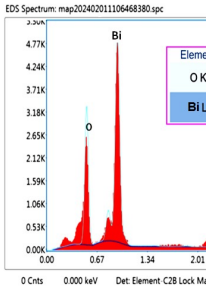

Fig. 5 (b)

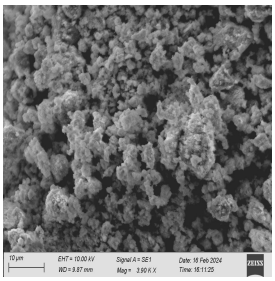

Fig. 5 (c)

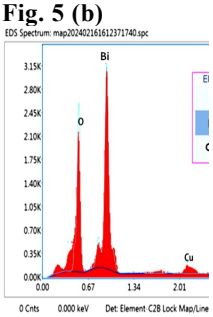

Fig. 5 (d)

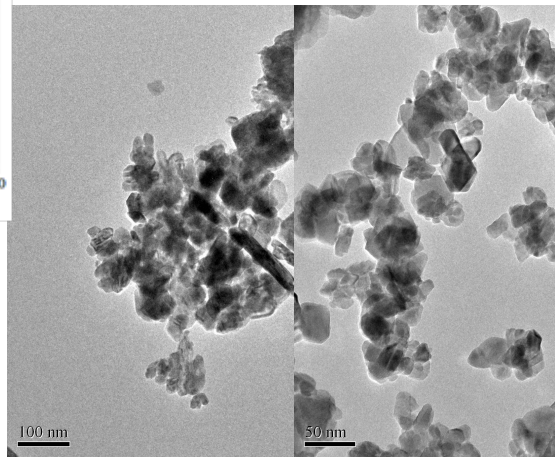

Fig. 6 (a)

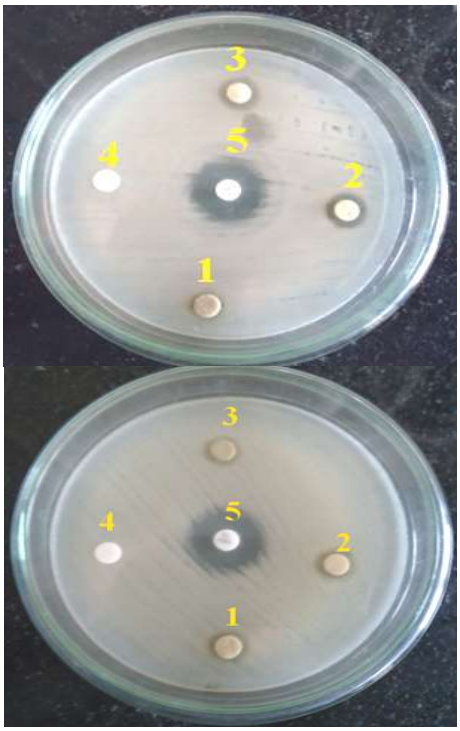

Fig. 7 (a)

Fig. 7 (b)

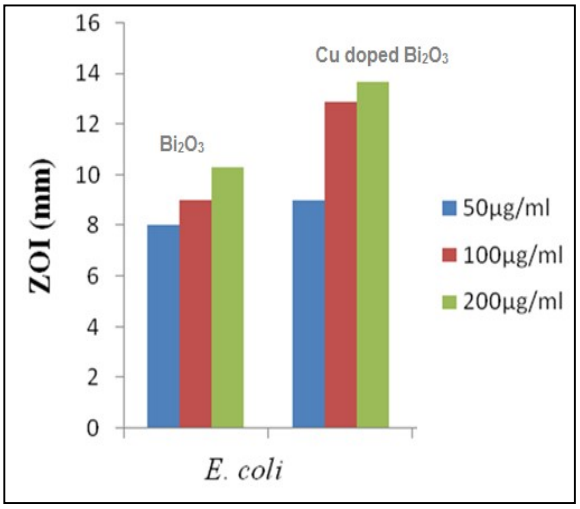

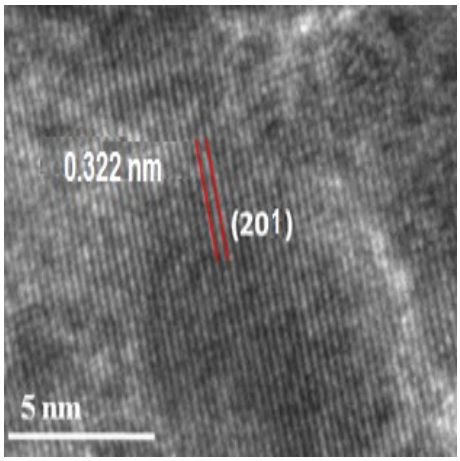

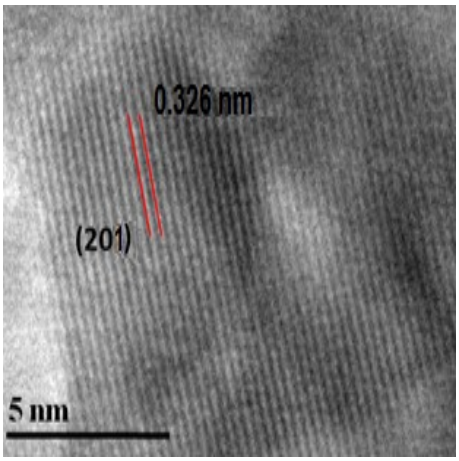

Fig. 7 (c)

Authors' Contributions

Dr. G. Lakshiminarayanan conceived and designed the study, supervised the research work, and contributed to data interpretation and manuscript preparation. The experimental work, including synthesis, characterization, and antibacterial studies, was carried out by the authors. All authors participated in data analysis, reviewed the results, contributed to manuscript revision, and approved the final version of the manuscript.

Funding

The authors received no specific funding for this research from any funding agency in the public, commercial, or not-for-profit sectors.

Competing Interests

The authors declare that they have no known competing financial interests or personal relationships that could have appeared to influence the work reported in this paper.

Data Availability

The data supporting the findings of this study are available from the corresponding author upon reasonable request.